Time-accurate blade surface static pressure behaviour on a rotating H-Darrieus wind turbine

Longhuan Du[1], Grant Ingram[2] , Robert G. Dominy[3]

Abstract

Time-accurate blade pressure distributions on a rotating H-Darrieus wind turbine at representative tip speed ratios during start-up are presented here which allow blade dynamic stall and laminar separation bubbles to be observed clearly and which provide a rare experimental demonstration of the flow curvature effect inherent in H-Darrieus turbine operation. The convection of a dynamic stall vortex along the blade surface at high reduced frequency has also been clearly identified. This study provides new information of the complex aerodynamics of the vertical axis wind turbines (VAWTs) and provides unique experimental data to validate the transient blade static surface pressure distribution predicted by CFD models. To the best of the authors' knowledge, this is the first time that the instantaneous pressure variation around the blade has been measured and recorded directly for an H-Darrieus wind turbine.

1. Introduction

Although the configuration of the H-Darrieus VAWT is simple (Figure 1), the flow physics are complex, particularly during the start-up phase when the blades experience all possible angles of attack leading to intermittent stall and significant flow curvature effects. Despite a resurgence of interest in VAWTs and numerous efforts to improve their efficiency, high quality experimental data remain scarce resulting in a limited number of appropriate test cases for CFD validation.

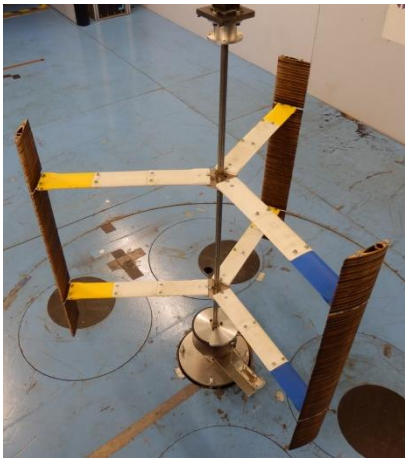

Figure 1: A typical three-bladed H-Darrieus wind turbine

The literature describes various analytical models that have been developed and applied (e.g.[1-8]) together with the use of CFD models (e.g.[9-17]) in order to better understand VAWT

Corresponding author: Longhuan Du (longhuan_du@163.com)
[1] School of Architecture and Environment, Sichuan University, Chengdu, China.
[2] Department of Engineering, Durham University, Durham, UK.
[3] Faculty of Engineering and Environment Department of Mechanical & Construction Engineering, Northumbria University, Newcastle, UK.

aerodynamics. Despite numerous studies our understanding of some fundamental aspects of VAWT performance remains incomplete. Experimental data are available but their scope has remained mostly restricted to overall power extraction with limited attention to the more difficult measurement and interpretation of the blade loading and underlying flow physics (e.g.[18-27]). Explanations of the turbine's performance have therefore been based mostly on simulation studies because of the difficulty of applying traditional measurement methods such as hot wires or pressure probes to the rotating turbine. It is only in recent years that researchers have had access to the computing power required to simulate the time-accurate flow physics in detail aided by the continued development of CFD and improved experimental capabilities such as particle image velocimetry (PIV) (e.g. [28-31]).
However, there have been no published studies of the time-accurate blade pressure distributions which arguably provide the most useful aerodynamic data. In this paper a time-accurate, on-board pressure measurement system was employed to measure directly the instantaneous pressure change around the blades of an H-Darrieus wind turbine when the machine was rotating at operational tip speed ratios. All of the measuring and recording components were placed on the turbine and rotated with the blades. The system was controlled remotely using Bluetooth communication.

2. Experimental configuration

2.1 The wind tunnel and the three-bladed H-Darrieus wind turbine

The tests were performed in the Durham University $2\ \mathrm{m}^2$, $3/4$ open-jet, open-return wind tunnel. More details about this wind tunnel can be found in reference[32,33]. Each turbine blade was attached to the vertical, central shaft by two support arms ($R = 300$ mm) and the whole turbine was centred in the wind tunnel test section in order to reduce boundary and ground effects. The 15 mm diameter central shaft was supported at both ends to minimise vibration at high turbine rational speeds and it was aligned vertically using a digital inclinometer within a tolerance of $\pm 0.05^{\circ}$. At its base the shaft was attached to a permanent magnet torque meter that could be used to apply load to the turbine and to measure its torque. The torque meter comprised a fixed lower aluminium disc to which were attached permanent magnets. The upper disc was free to rotate with the turbine. Changing the inter-disc spacing by raising or lowering the lower disc produced a corresponding change of load resistance. This torque meter was used to provide 'brake' torque which together with a drive motor to provide an accelerating torque enabled a constant rotational speed to be maintained over a wide range of operating conditions including some that could not normally be achieved by a VAWT under normal conditions.

2.2 On-board pressure measurement system

2.2.1 The blades

The blade profile that was chosen for this study was the NACA0021 since symmetric NACA series blades have been widely used in VAWT research (e.g.[10,14,34]) and the NACA0021 profile has a relatively large thickness to accommodate the pressure tappings and internal components. The chord length was $c = 100$ mm and blade span was $S = 700$ mm. Each blade was assembled from a set of laser cut plywood laminates of 10 mm width. Alignment of the laminates was achieved by assembling them onto two bars which passed through holes cut into the laminates. In order to reduce their mass, the blades had central material removed but retained a significant wall thickness to maintain strength and stiffness. In addition to the wooden laminates a single perspex laminate was constructed which housed 15 surface static pressure tappings (**Figure 2**). Fourteen of the pressure tappings were distributed

symmetrically on the pressure side and suction side with one tapping at the leading edge. The coordinates of these pressure tappings are shown in **Figure 3**. Due to the relatively small thickness near the blade trailing edge it was not possible to locate any tappings downstream from $x/c = 0.6$ on the respective surfaces. The tappings were created by drilling holes perpendicular to the local blade surface into transverse internal tubes. Each pressure tapping had a diameter of 0.5 mm.

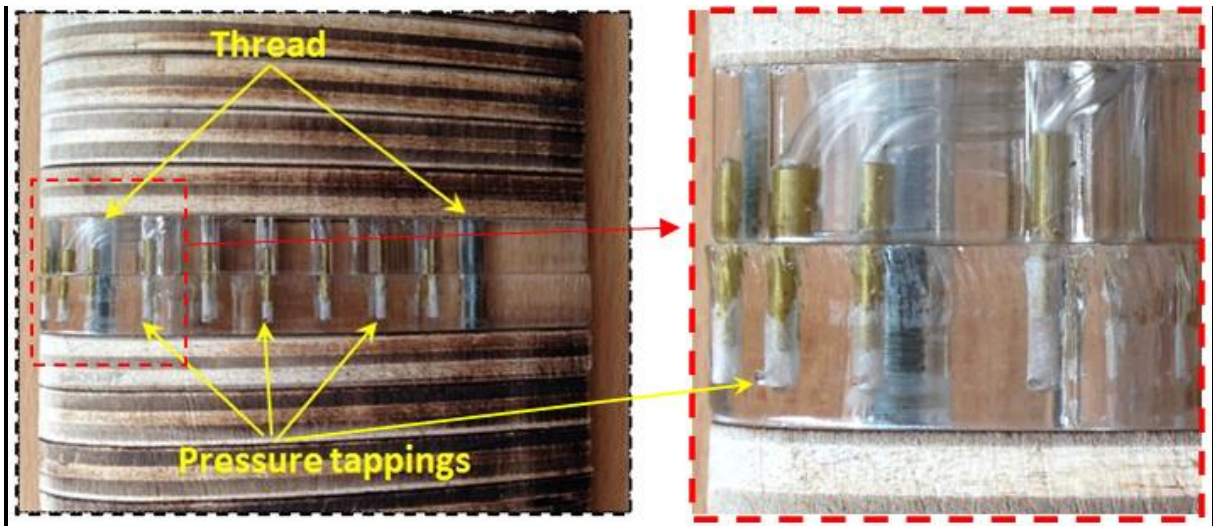

(a) (b)

Figure 2 (a) The NACA0021 blade with the pressure tapping section made from perspex, (b) closed-up view at the leading edge.

The laminate with the pressure tappings was placed at the blade's mid-span although the laminated construction method provides the option to place the instrumented section at different spanwise locations for future studies (**Figure 2**). Each pressure tapping was connected by a short length of pneumatic tubing to the on-board pressure scanner.

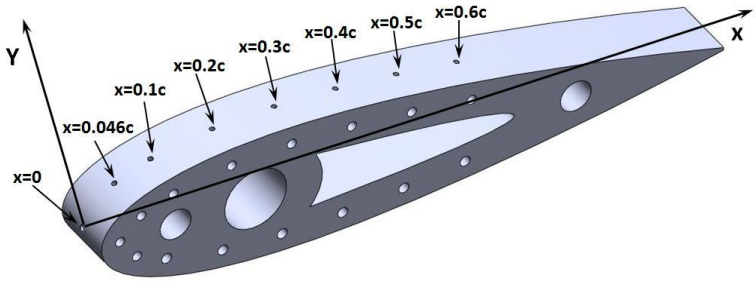

Figure 3 Instrumented Blade Section showing the pressure tapping coordinates on the top surface. The pressure scanner

A 16-channel miniature electronic pressure scanner, ESP-16HD, was employed in this study to convert pressure into an analog electrical signal. The outputs from the sensors are electronically multiplexed through a single on-board instrumentation amplifier at rates up to 20,000 Hz. Each channel was calibrated using a micro-manometer and the calibration data for each channel of the scanner could be reduced into offset, sensitivity and non-linearity coefficients that were used to determine the pressures from the measured voltages. In this study, a fourth-order polynomial resulting from a five-point calibration was used to calculate

the pressure during data acquisition as suggested by the manufacturer[35]. A linear function was found for each channel and the static error for the fourth-order correction was within $\pm 0.05\%$ of the full scale pressure range (± 2.5 kPa).

The pressure channels on the scanner were connected to the corresponding pressure tappings on the blade using 500 mm long, 1 mm ID flexible tubing. The reference pressure input for the scanner was provided by a separate tube with one end fastened on the centre shaft and located outside the wind tunnel jet. Initial tests demonstrated that the reference pressure input did not vary under different turbine rotational speeds. The reference pressure input value for each test was also recorded by scanner channel No.16 for use in calibrating the results from other 15 channels during the data post-processing.

It is well known that the use of tubing to connect the blade surface static pressure tappings to the pressure scanner can influence the system response. For pressure fluctuations close to the natural frequency of the system this can lead to signal amplification whereas at higher frequencies the signal may be attenuated. Studies have shown that for tubing configurations similar to those used in this study it is possible to determine and apply phase and amplitude corrections for measurement frequencies up to around 200 Hz (e.g.[36,37]). However, for the range of frequencies of the significant aerodynamic events that were observed during the turbine's rotation, the transfer function correction data of Sims-Williams[36] shows that for this system of tubing and pressure tapping geometry the required amplitude (max +/- 5%) and phase corrections are small. Consequently they have not been applied to these data although it is acknowledged that some high frequency but small scale features might have been attenuated.

2.2.2 The microcontroller datalogger system

The microcontroller datalogger developed in this study was based on an Olimexino-STM32 board. This is an Arduino-based system which can be powered by a single Li-Po battery and can save data to a MicroSD card as can be seen in Figure 4.

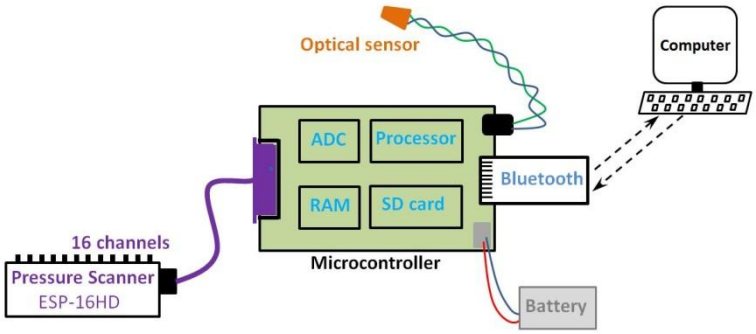

Figure 4 Schematic diagram of the microcontroller datalogger and other components

In this study, the microcontroller was controlled wirelessly by a laptop located outside the wind tunnel using the Bluetooth short-range wireless connectivity standard. Users were able to modify the sample rate, sample time and scanner channel number during testing without stopping the turbine. The output data from the pressure scanner was recorded in conjunction with signals from an optical sensor to determine the rotor position and speed. Each time the blade with the pressure tappings passed the azimuth angle, $\theta = 0^{\circ}$, a pulse (TTL voltage output) would be generated from the optical sensor and transmitted to the microcontroller. This pulse would cause the microcontroller to stop and record a new set of data. Knowing the physical starting position of each dataset, this arrangement allowed all the pressure data to be mapped back to the blade position (azimuth angle) for each revolution when it was processed.

The time delay between detecting the active pulse edge from the optical sensor and writing the new set of data to the MicroSD card was 5 microseconds and the azimuth angle shift resulting from this delay was considered during data post-processing.

To enable the full range of tip speed ratios to be measured in the wind tunnel and especially to capture data for tip speed ratio (λ) values above peak power it was necessary to drive the turbine electrically. Constant rotational speed, when required, was achieved by using the motor/torque meter combination. The blade pressures were measured channel by channel with an appropriate constant pre-set time interval (based on tip speed ratio) which equated to $\theta = 0.25^{\circ}$ leading to $360^{\circ}/0.25^{\circ} = 1{,}440$ points being measured for each revolution. The measurements were phase averaged over N revolutions for each channel in order to calculate the averaged pressure value at each azimuth angle and minimise any noise from the electronic components. The number of revolutions, N, was determined by the sensitivity study detailed in the following section. Some typical sample rates are presented in Table 1.

Fixed tip speed ratio	Upstream wind speed (m/s)	Fixed motor speed (Hz)	Time step (degree)	No. of sample points per revolution	Fixed sample frequency (Hz)
0.5	7	1.856	$\theta = 0.25^{\circ}$	1,440	2673
0.8	7	2.971	$\theta = 0.25^{\circ}$	1,440	4278
1	7	3.714	$\theta = 0.25^{\circ}$	1,440	5348
1.5	7	5.57	$\theta = 0.25^{\circ}$	1,440	8021
2	7	7.427	$\theta = 0.25^{\circ}$	1,440	10695

Table 1 Typical parameters used in this study for on-board pressure measurement with turbine radius $R = 300$ mm, $c = 100$ mm, $n = 3$

2.2.3 Instrumentation mounting arrangement

The microcontroller datalogger (including the battery) and pressure scanner were placed close to the turbine centre shaft in order to reduce their effect on the flow. A laser diode was used to ensure the optical sensor generated the pulse signal when the instrumented blade passed the azimuth angle of $\theta = 0^{\circ}$.

2.3 Data post-processing

2.3.1 On-board pressure measurement data interpolation

The time interval between each measurement was pre-set to record 1,440 points for one revolution (a constant angular step of $\theta = 0.25^{\circ}$). In reality the nominally constant rotational turbine speed would vary by up to $\pm 1\%$ RPM resulting in slightly more or less than the nominal 1,440 points measured in one revolution. However due to the synchronised signal from the optical sensor, the first point recorded by the datalogger would always occur at $\theta = 0^{\circ}$ and knowing the instantaneous rotational speed the positions of subsequent pressure measurements could be corrected easily using the process shown in Figure 5.

Revolution X		
Actual number of measured points	**Actual measured position /θ**	**value**
1432	0°	993
Actual step	0.2514°	999
$\theta = 0.2514^{\circ}$	0.5028°	998
	0.7542°	997
	⋮	⋮
	358.9992°	999
	359.2506°	998
	359.502°	998
	359.7534°	997

Revolution X	
Designed position /θ	**Interpolated value**
0°	993
0.25°	998.9333
0.5°	998.0167
0.75°	997.0222
⋮	⋮
359°	998.9833
359.25°	998
359.5°	997.9944
359.75°	997.0002

Figure 5 Example of on-board pressure measurement data interpolation process

2.3.2 Determining the number of revolutions and measurement uncertainty

In order to minimize the effect of any unwanted ambient electrical noise generated or picked up by the electronic components and any disturbance from upstream flow and wake, the pressure measurement for each pressure tapping (scanner channel) was repeated for N revolutions in order to calculate the mean pressure value at each azimuth angle. Consequently, although individual measurements were time-accurate, the data presented here are azimuthally averaged. A sensitivity study was performed to examine the number of revolutions required to produce a reliable result with low standard deviation. Five azimuth angles ($\theta = 10^{\circ}$, $\theta = 30^{\circ}$, $\theta = 100^{\circ}$, $\theta = 200^{\circ}$ and $\theta = 300^{\circ}$) were selected as examples.

It was demonstrated that after approximately 100 turbine revolutions the standard deviation (SD) for all five azimuth angles became relatively stable and that further increasing the number of measured revolutions and sampling time did not significantly improve the data quality (more detail about the sensitivity study can be found in reference[32]). Moreover, it was found that even averaging over only 10 revolutions the noise for the curve of pressure against azimuth angle is very limited, especially for the blade un-stalled region, and that a further increase by an order of magnitude reduced it to negligible level as shown in Figure 6. Therefore, in this study the on-board pressure measurement for each scanner channel/tapping was repeated for 100 revolutions.

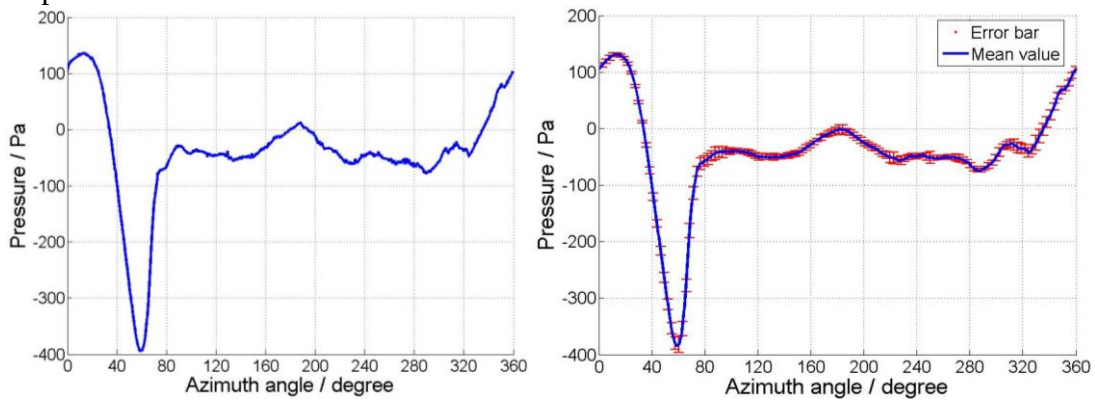

(a) (b)

Figure 6 Measured pressure variation against azimuth angle for scanner channel 1. (a) Phase averaged value over 10 revolutions. (b) Phase averaged value over 100 revolutions with error bars.

An uncertainty study was carried out and the largest uncertainty of the measured pressure was found to correspond to 2% of the peak pressure coefficient (*Cpp*). It should be noted that this apparently high value is a consequence of pressures in this study being non-dimensionalized by the upstream wind speed (V) rather than the much higher but cyclic resultant speed (V_r), especially at relative large tip speed ratio. This non-dimensionalisation by the free stream dynamic head is commonly used for studying dynamic problems in the literature (e.g.[38,39]).

3. Results

The instantaneous blade pressure distribution and its variation during turbine rotation were measured at a number of tip speed ratios. Three typical tip speed ratios are presented for this particular high solidity turbine, low $\lambda = 0.5$; medium $\lambda = 1.5$; high $\lambda = 2.0$. These tip speed ratios are representative of the turbine during start-up. The sign convection in this study is shown in Figure 7.

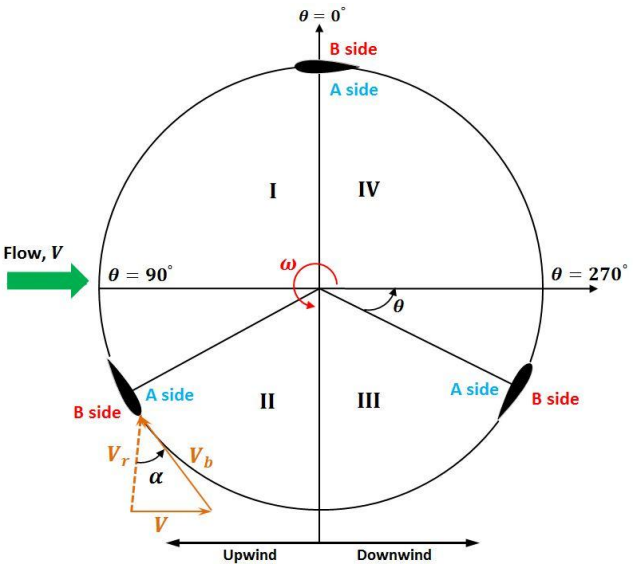

Figure 7 Sign convection for on-board pressure measurement study

The blade's inner surface (facing the axis) is abbreviated as side A while the B side is defined as the blade's outer surface as shown in Figure 7. A theoretical incidence angle, α is calculated based on the turbine kinematics after Worasinchai[40]. This simple kinematic analysis does not take any blade loading, wake, flow curvature or rotor effects into consideration and it assumes a uniform flow through the whole domain but it provides a useful first approximation of the nominal incoming flow angle. Because the kinematic analysis is based only on the position and speed of the blade it is independent of the blade design and therefore it also provides a useful reference when comparing blades of different geometry. For the following parts of the paper, this theoretical incidence angle is referred as incidence angle, α. Of particular interest in this study were the capture of blade dynamic stall, laminar separation bubbles and blade path curvature effects.

3.1 Blade Surface Pressure distribution at $\lambda = 0.5$

The results at the lowest tip speed ratio of $\lambda = 0.5$ are presented first in Figure 8. It can be seen that at this relatively low tip speed ratio the pressure distribution measured from this symmetrical aerofoil occurs not at $\theta = 0^{\circ}$ but at approximately $\theta = 5^{\circ}$. This differs from the kinematic analysis that assumes symmetry when the blade is parallel to flow at $\theta = 0^{\circ}$. This difference is caused by the turbine's rotation which leads to curvature effects becoming significant. A curvilinear flow results in a symmetrical blade becoming virtually cambered as pointed out by Migliore et al.[41]. It could also be argued that a small positional error might result from the inaccurate alignment of the blade with the upstream flow. However, even the maximum possible alignment error ($\theta = \theta \pm 2^{\circ}$) is not enough to cause this observed effect.

The blade incidence angle α further increases with the increase of azimuth angle θ and the blade's **A** side becomes the suction side while the **B** side becomes the pressure side (the resultant flow approaches from the **B** side after $\theta > 5^{\circ}$). According to static wind tunnel measurements (e.g.[42]), a laminar separation bubble forms at the blade trailing edge which moves towards the leading edge as the angle of attack increases. However since there was no pressure tapping at the blade trailing edge in this study, the laminar separation bubble is not captured until $\theta = 15^{\circ}$, around a blade position of $0.4c \sim 0.6c$ (**A** side). It becomes more apparent at $\theta = 25^{\circ}$ where the bubble separation and re-attachment positions are around $0.3c$ and $0.5c$ respectively. It should be noted that due to the limited number of pressure tappings, the location of the bubble separation and re-attachment positions are not exact.

The maximum negative pressure coefficient for the blade suction side (**A** side) continues to decrease with the increase of azimuth angle from $C_{pp} = -4.5$ at $\theta = 25^{\circ}$ to $C_{pp} = -10$ at $\theta = 45^{\circ}$. At this stage the blade generates significant torque due to the increasing lift force (shown in **Figure 9**) and the laminar separation bubble moves further towards the leading edge along with the reduction of bubble length. Within the limit of the resolution provided by the finite number of pressure tappings, the laminar separation bubble can be identified at around $0.1c \sim 0.2c$ for $\theta = 35^{\circ}$ and $\theta = 45^{\circ}$ (see Figure 8). It must be noted that at $\theta = 45^{\circ}$, the theoretical incidence angle is about $\alpha = 30^{\circ}$ which is already far beyond the static stall angle of $\sim 13^{\circ}$ (NACA0021) at similar Reynolds numbers[43,44]. Even taking the curvature effect into consideration, the dynamic stall effect which significantly delays the stall angle is successfully captured in this study. The laminar separation bubble bursts when the blade reaches about $\theta = 50^{\circ}$ showing pressure fluctuation at the leading edge and the blade totally stalls at around $\theta = 55^{\circ}$, resulting in a significant decrease of lift force and a sudden change of blade torque coefficient as demonstrated in **Figure 9**. The stalled blade produces zero or or limited positive torque in quadrant II and quadrant III.

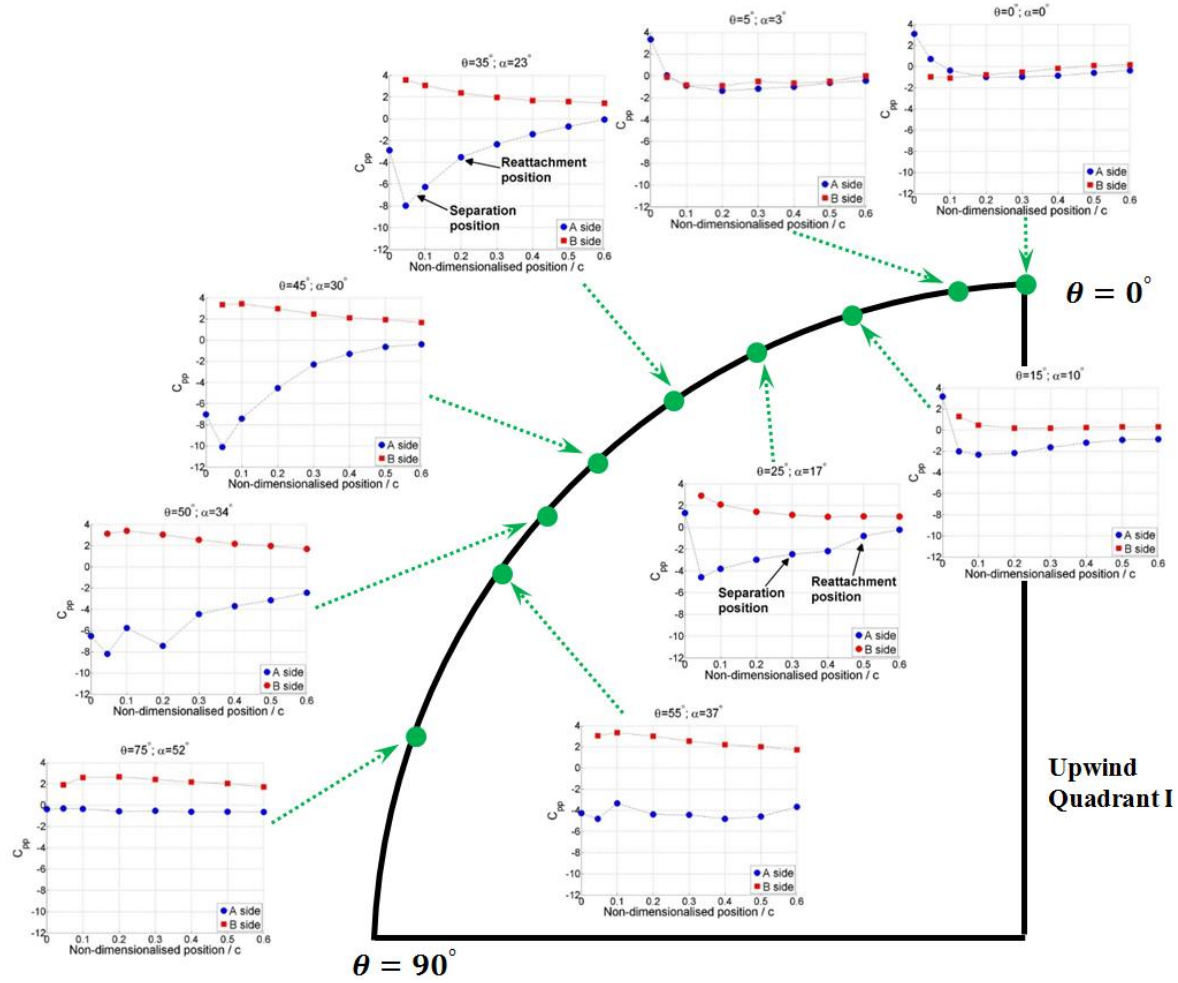

Figure 8 Instantaneous blade pressure measurements in the upwind quadrant I. $R = 300$ mm, $c = 100$ mm, $n = 3$, $\lambda = 0.5$, $V = 7$ m/s.

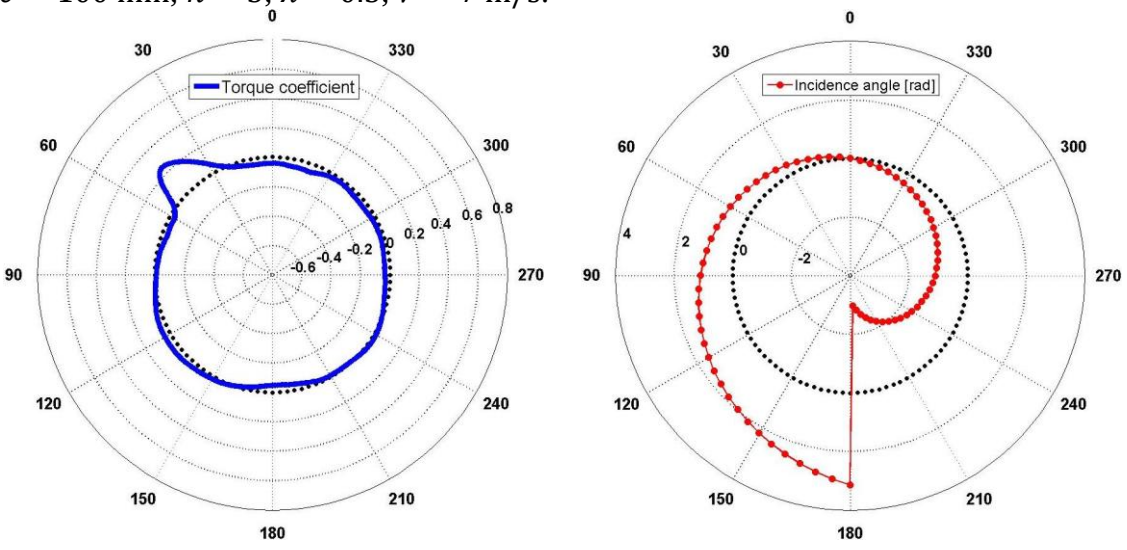

Figure 9 (a) Torque coefficient. (b) Theoretical incidence angle. $R = 300$ mm, $c = 100$ mm, $n = 3$, $\lambda = 0.5$, $V = 7$ m/s. (Note: since at this low tip speed ratio the blade will experience all possible incidence angle from $\alpha = -180^{\circ}$ to $\alpha = 180^{\circ}$, the radius axis for incidence angle data is significantly larger than that for torque coefficient data. Therefore these two data sets are presented separately)

The results for the blade behaviour in the downwind quadrant (quadrant IV) are presented in Figure 10. From a quasi-steady consideration of a symmetrical blade, its behaviour in quadrant IV would be expected to mirror that in quadrant I except the flow comes from the A side which becomes the pressure side while the B side becomes the suction side. However it can be seen that the blade still stalls at $\theta = 325^{\circ}$ ($\alpha = -23^{\circ}$) due to the dynamic hysteresis, which delays the onset of flow reattachment. This is consistent with the recent study performed by Balduzzi et al.[45] who also captured the dynamic hysteresis experimentally and numerically by pitching the NACA0021 blade. The flow subsequently reattaches on the suction side (B side) at low enough incidence when the turbine reaches $\theta = 345^{\circ}$ and no laminar separation bubble is captured in quadrant IV. No useful torque is generated by the blades in quadrant IV and a conclusion can be safely drawn that at low tip speed ratios the turbine driving force (torque) is mainly generated by the blade in quadrant I.

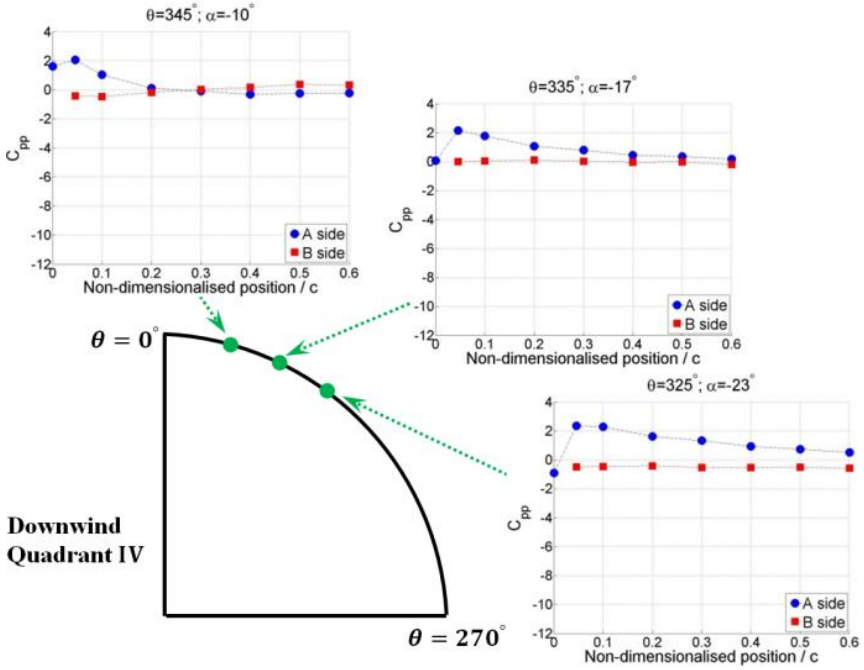

Figure 10 Instantaneous blade pressure measurements in the downwind quadrant IV. $R = 300$ mm, $c = 100$ mm, $n = 3$, $\lambda = 0.5$, $V = 7$ m/s.

3.2 Pressure distribution at $\lambda = 1.5$

At the medium tip speed ratio of $\lambda = 1.5$, the blade incidence range is significantly reduced. However the curvature effect becomes more pronounced and the blade zero incidence (symmetrical pressure distribution) occurs at $\theta = 24^{\circ}$ while the theoretical angle of attack at this position is $\alpha = 10^{\circ}$ as shown in Figure 11. The resultant flow still approaches from the blade's A side at the geometrical zero position of $\theta = 0^{\circ}$ indicating the symmetrical blade is again virtually cambered. When the blade reaches $\theta = 45^{\circ}$, a laminar separation bubble is then captured around $0.4c \sim 0.6c$. Increasing the angle of incidence causes the separation bubble to move forward and to reduce in length and the bubble is captured around blade $0.1c \sim 0.2c$ at $\theta = 70^{\circ}$.

An interesting phenomenon is observed when the turbine reaches $\theta = 90^{\circ}$. The pressure measurements demonstrate that the peak negative pressure point starts to traverse along the blade surface from $\theta = 90^{\circ}$. As can be seen in Figure 11 the corresponding peak

suction points for $\theta = 90^{\circ}$, $\theta = 95^{\circ}$, $\theta = 100^{\circ}$, $\theta = 105^{\circ}$ and $\theta = 110^{\circ}$ are around $0.05c$, $0.25c$, $0.35c$, $0.45c$ and $0.6c$. This wave-like C_{pp} distribution illustrates that the dynamic-stall vortex formed at the blade leading edge convects along the blade as the incidence (azimuth angle) keeps increasing. This vortex is finally shed into the wake after $\theta = 110^{\circ}$ (since there is no pressure tapping after $0.6c$, it is not possible to know the exact θ). It seems that this dynamic stall vortex is not the laminar separation bubble captured at lower incidence (azimuth angle) since the maximum pressure coefficient at the beginning of convection of $\theta = 95^{\circ}$ is only $C_{pp} = -14$ while the laminar separation bubble has a peak value of $C_{pp} = -22$ around $= 70^{\circ}$. A more reasonable explanation is that the laminar separation bubble bursts around $\theta = 90^{\circ}$ and a new dynamic vortex with lower strength is then formed at the blade leading edge due to the fast rotation (reduced frequency). This newly formed vortex also might be part of the burst laminar separation bubble.

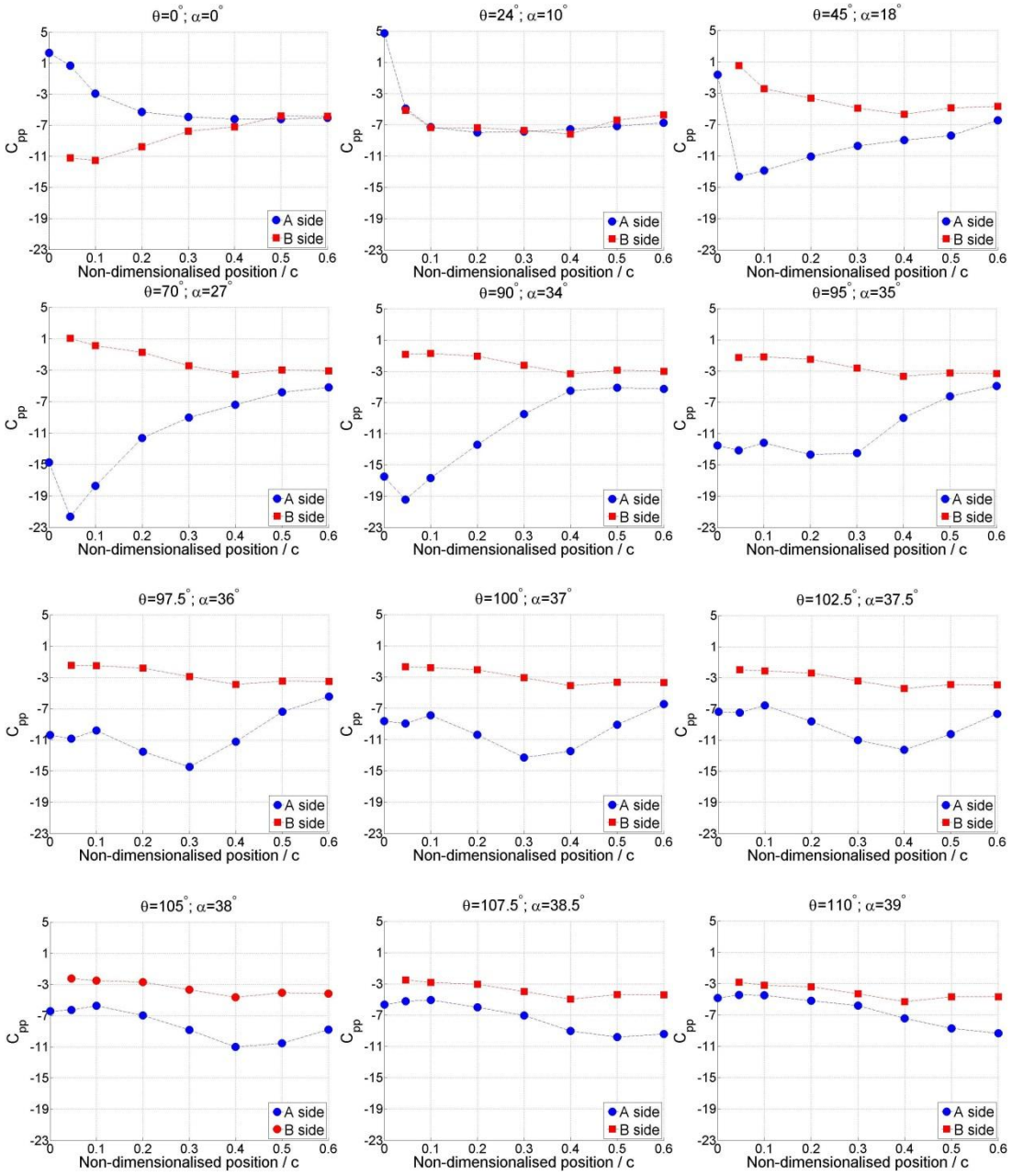

Figure 11 Instantaneous blade pressure measurements in the upwind quadrant I and quadrant II. $R = 300$ mm, $c = 100$ mm, $n = 3$, $\lambda = 1.5$, $V = 7$ m/s.

A previous study performed by Worasinchai[40] also captured the dynamic vortex convection along the blade surface by purely pitching the blade. Worasinchai claimed that the strength of the dynamic stall vortex increases with the increase of reduced frequency of pitching and the blade stall angle is considerably delayed at the highest reduced frequency examined ($k = 0.25$). For H-Darrieus wind turbine operation, the reduced frequency can be also defined as $k = \frac{c}{2R}\lambda$ [32]. Therefore, the corresponding reduced frequency for the above two tip speed ratios examined here, $\lambda = 0.5$ and $\lambda = 1.5$, are $k = 0.08$ and $k = 0.25$ respectively.

For pressure measurement at $\lambda = 0.5$ ($k = 0.08$), as shown in Figure 8, the dynamic vortex convection is not captured (or not clearly captured). The laminar separation bubble bursts at $\theta = 50^{\circ}$ and the blade totally stalls at $\theta = 55^{\circ}$. This might be because at this low tip speed ratio (low reduced frequency), the strength of the dynamic vortex is too low to attach and convect on the blade surface and is quickly shed into the wake. In contrast, at $\lambda = 1.5$ ($k = 0.25$) the dynamic stall vortex is finally shed into the wake after the blade travels through more than 20° (azimuth angle).

With respect to the torque, the measurements illustrate the blade can only produce limited torque in quadrant III and quadrant IV while most of the useful torque is generated by the blade in the upwind regions of quadrant I and quadrant II as illustrated in Figure 12. At this medium tip speed ratio, blade net torque is considerably increased compared with that at the lower tip speed ratio of $\lambda = 0.5$, indicating a fast turbine accelerating period..

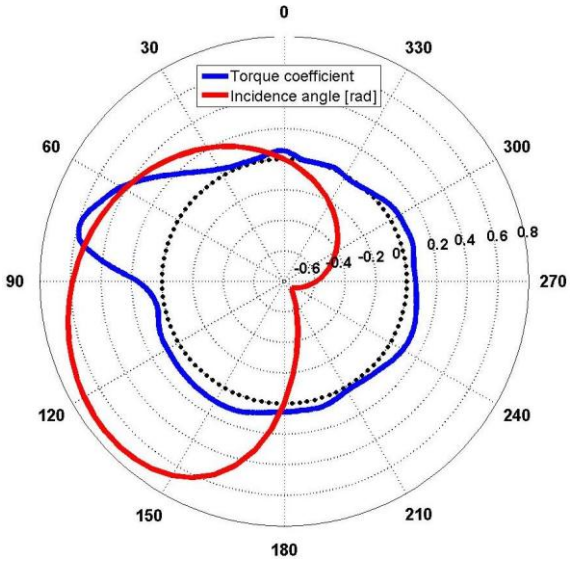

Figure 12 Torque coefficient and theoretical incidence angle. $R = 300$ mm, $c = 100$ mm, $n = 3$, $\lambda = 1.5$, $V = 7$ m/s.

3.3 Pressure distribution at $\lambda = 2.0$

Pressure measurements were also performed at the relatively high tip speed ratio of $\lambda = 2.0$ and the results are shown in Figure 13. A polar plot of torque and incidence in radians is in the centre of the figure with blade pressure distributions at key azimuthal positions around the outside. With the further increase of turbine rotational speed, the curvature impact is also exacerbated as the pressure symmetry in the upwind region is captured at an azimuth angle

around $\theta = 33^{\circ}$. After $\theta = 33^{\circ}$, the resultant flow is incident upon the blade B side which becomes the pressure side while the A side becomes the suction side. Meanwhile a laminar separation bubble is captured at $\theta = 60^{\circ}$ around blade position of $0.4c \sim 0.6c$. This laminar separation bubble moves further towards the leading edge at $\theta = 80^{\circ}$ and $\theta = 100^{\circ}$ along with the increase of incidence. Since the high tip speed ratios significantly reduce the incidence range that the blade will experience (shown in Figure 13), the theoretical angle of attack actually starts to decrease at around $\theta = 140^{\circ}$ compared with that at $\theta = 100^{\circ}$. The measured pressure distribution also demonstrates that the blade does not stall at $\theta = 140^{\circ}$ but experiences a lower peak pressure coefficient of $C_{pp} = -13.5$ compared with $C_{pp} = -25.5$ at $\theta = 100^{\circ}$. The torque coefficient also demonstrates that there is no sudden blade torque change but the variation is smooth during the whole revolution. Moreover the effective angle of attack becomes zero again at an azimuth angle of $\theta = 165^{\circ}$, although the theoretical calculation indicates the incidence angle is approximately $\alpha = 14^{\circ}$. After that, the resultant flow is incident upon the blade's A side as can be seen at $\theta = 225^{\circ}$ and $\theta = 325^{\circ}$. The turbine produces considerable power at this high tip speed ratio since the blade does not stall for the whole revolution and torque can be generated at all azimuth angles. These results are consistent with the recent study performed by Blondel et al.[27] who demonstrate the flow will always attach to the blade at high tip speed ratio and no dynamic stall is observed. However, it must be noted that the peak negative torque in the downwind region is only around $C_{pp} = -18$ ($\theta = \sim 210^{\circ}$) which is significantly lower than that of $C_{pp} = -26$ ($\theta = \sim 100^{\circ}$) in the upwind region. This lower peak negative pressure coefficient in the downwind region demonstrates that the majority of the torque is generated by the blade in the upwind region, which can also be seen from the torque coefficient radar distribution. Moreover, since the pressure tappings were placed at mid-span where there are no or limited tip loss effects, the torque coefficient for the whole 3D blade will be less than that shown in **Figure 13**.

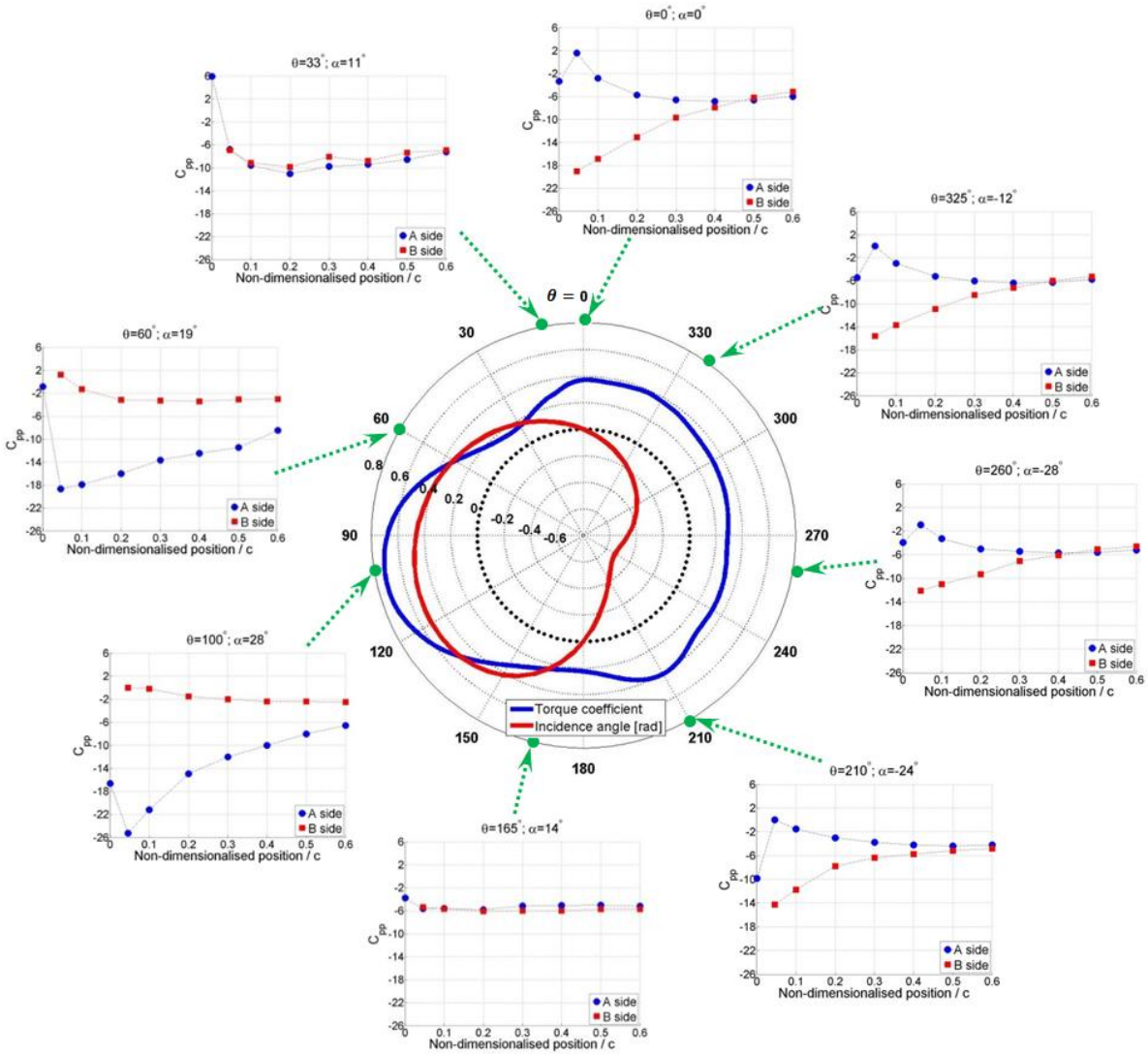

Figure 13 Instantaneous blade pressure measurements for the whole revolution. $R = 300$ mm, $c = 100$ mm, $n = 3$, $\lambda = 2.0$, $V = 7$ m/s.

4. Conclusions

A time-accurate on-board pressure measurement system was successfully developed and employed in this study to measure the instantaneous blade pressure distribution and its variation during the rotation of an H-Darrieus wind turbine. The three-bladed turbine was driven at constant tip speed ratios by a motor in conjunction with a torque meter providing a stabilizing 'brake' resistance. The blade surface static pressures were measured together with signals from an optical sensor enabling the data collected to be mapped back to the blade position (azimuth angle) for each revolution. Dynamic stall and laminar separation bubbles were clearly captured along with the flow curvature effect. Furthermore, the convection of the dynamic stall vortex along the blade surface at large reduced frequency was also clearly identified. The instantaneous pressure measurements indicate that the dynamic stall vortex can only convect along the blade surface at high reduced frequency. At low tip speed ratio, the vortex is too weak to attach and convect along the surface resulting in an earlier blade stall and less torque being generated in the upwind region.

This study provides new knowledge and understanding of the complex aerodynamics of the H-Darrieus wind turbine and this unique data provides a dedicated test case for the

validation of unsteady CFD models. To the best of the author's knowledge, this is the first time that this technique has been used in the study of H-Darrieus wind turbines.

Acknowledgement

The authors would like to thank the technical staff Collin Wintrip, Gary Parker and Simon Apps in the School of Engineering and Computing Sciences of Durham University for their help in setting up the experiments. The authors would also like to thank Mr Peter Baxendale at Durham University for helping to build and setup the on-board pressure measurement system. This work was funded by the Sichuan Science and Technology Program (No.2018JY0595).

Reference

1. Tai F, Kang KW, Jang MH. Study on the analysis method for the vertical-axis wind turbines having Darrieus blades. *Renewable Energy.* 2013;54(6):26-31.

2. Saeidi D, Sedaghat A, Alamdari P, Alemrajabi AA. Aerodynamic design and economical evaluation of site specific small vertical axis wind turbines. *Applied Energy.* 2013;101(1):765-775.

3. Svorcan J, Komarov D, Peković O, Kostić I. Aerodynamic design and analysis of a small-scale vertical axis wind turbine. *Journal of Mechanical Science & Technology.* 2013;27(8):2367-2373.

4. Bedon G, Castelli MR, Benini E. Optimization of a Darrieus vertical-axis wind turbine using blade element – momentum theory and evolutionary algorithm. *Renewable Energy.* 2013;59(11):184-192.

5. Roh S, Kang SH. Effects of a blade profile, the Reynolds number, and the solidity on the performance of a straight bladed vertical axis wind turbine. *Journal of Mechanical Science & Technology.* 2013;27(11):3299-3307.

6. Paraschivoiu I. Double-Multiple Streamtube Model for studying Vertical Axis Wind Turbine. *Journal of Propulsion and Power.* 1987;4(4):370-377.

7. Templin R. Aerodynamic Performance Theory for the NRC Vertical-Axis Wind Turbine. *National Research Council of Canada. Laboratory technical report ; LTR-LA-160.* 1974.

8. Strickland J. The Darrieus Turbine: A Performance Prediction Model Using Multiple Streamtubes. *Sandia National Laboratories Technical Report SAND75-0431.* 1975.

9. Bianchini A, Balduzzi F, Ferrara G, Ferrari L. Virtual incidence effect on rotating airfoils in Darrieus wind turbines. *Energy Conversion and Management.* 2016;111:329-338.

10. Castelli M, Englaro A, Benini E. The Darrieus Wind Turbine: Proposal for a New Performance Prediction Model Based on CFD. *Jornal of Energy.* 2011;36(8):4919-4934.

11. Danao L, Edwards J, Eboibi O, Howell R. A numerical investigation into the influence of unsteady wind on the performance and aerodynamics of a vertical axis wind turbine. *Applied Energy.* 2014;116:111-124.

12. Li S, Zhu S, Xu YL, Xiao Y. 2.5D large eddy simulation of vertical axis wind turbine in consideration of high angle of attack flow. *Renewable Energy.* 2013;51(2):317-330.

13. Mohamed M. Performance Investigation of H-Rotor Darrieus Turbine With New Airfoil Shapes. *Journal of Energy.* 2012;47(1):522-530.

14. Rossetti A, Pavesi G. Comparison of Different Numerical Approaches to the Study of the H-Darrieus Turbines Start-Up. *Journal of Renewable Energy.* 2013;50(0):7-19.

15. Velascoa D, Mejia OL, Laín S. Numerical simulations of active flow control with synthetic jets in a Darrieus turbine. *Renewable Energy.* 2017;113:129-140.

16. Wang S, Ingham DB, Ma L, Pourkashanian M, Tao Z. Numerical investigations on dynamic stall of low Reynolds number flow around oscillating airfoils *Computers and Fluids.* 2010;39(9):1529-1541.

17. Zamani M, Nazari S, Moshizi SA, Maghrebi MH. Three dimensional simulation of J-shaped Darrieus vertical axis wind turbine. *Energy.* 2016;116:1243-1255.

18. Danao L, Eboibi O, Howell R. An experimental investigation into the influence of unsteady wind on the performance of a vertical axis wind turbine. *Applied Energy.* 2014;116(3):111-124.

19. Edwards J, Danao LA, Howell RJ. Novel Experimental Power Curve Determination and Computational Methods for the Performance Analysis of Vertical Axis Wind Turbines. *Journal of Solar Energy Engineering* 2012;134(3).

20. Howell R, Qin N, Edwards J, Durrani N. Wind Tunnel and Numerical Study of a Small Vertical Axis Wind Turbine. *Renewable Energy.* 2010;35(2):412-422.

21. Kim D, Gharib M. Efficiency improvement of straight-bladed vertical-axis wind turbines with an upstream deflector. *Journal of Wind Engineering & Industrial Aerodynamics.* 2013;115:48–52.

22. Klimas P, Worstell M. Effects of blade preset pitch/offset on curved-blade Darrieus vertical axis wind turbine performance. *Technical Report No.SAND81-1762, Sandia National Laboratories, USA.* 1981.

23. Mclaren K, Tullis S, Ziada S. Measurement of high solidity vertical axis wind turbine aerodynamic loads under high vibration response conditions. *Journal of Fluids and Structures.* 2012;32(3):12-26.

24. Sheldahl R, Klimas PC, Feltz LV. Aerodynamic Performance of a 5-metre Diameter Darrieus Turbine With Extruded NACA-0015 Blades. *Technical Report No. SAND80-0179, Sandia National Laboratories, USA.* 1980.

25. Dodd H, Ashwill TD, Berg DE, Ralph ME, Stevenson WA, Veers PS. Test Results and Status of the DOE/Sandia 34m Test Bed. *The Canadian Wind Energy Association Conference.* 1989.

26. Blackwell B, Sheldahl RE, Feltz LV. Wind Tunnel Performance Data for the Darrieus Wind Turbine with NACA0012 Blades. *Sandia Laboratories, SAND76-0130, United States.* 1977.

27. Blondel F, Galinos C, Paulsen U, Bozonnet P, Cathelain M, Ferrer G, Madsen HA, Pirrung G, Silvert F. Comparison of Aero-Elastic Simulations and Measurements Performed on NENUPHAR's 600kW Vertical Axis Wind Turbine: Impact of the Aerodynamic Modelling Methods. *IOP Conf. Series: Journal of Physics: Conf. Series 1037* 2018.

28. Buchner A, Lohry MW, Martinelli L, Soria J, Smits AJ. Dynamic stall in vertical axis wind turbines: Comparing experiments and computations. *Jornal of Wind Engineering and Industrial Aerodynamics.* 2015;146:163-171.

29. Ferreira C, Kuik GV, Bussel GV, Scarano F. Visualization by PIV of dynamic stall on a vertical axis wind turbine. 2009;46(1):97-108.

30. Fujisawa N, Shibuya S. Observations of dynamic stall on Darrieus wind turbine blades. *Journal of Wind Engineering and Industrial Aerodynamics.* 2001;89(2):201-214.

31. Tescione G, Ragni D, He C, Ferreira CJS, Bussel GJWV. Near wake flow analysis of a vertical axis wind turbine by stereoscopic particle image velocimetry. *Renewable Energy.* 2014;70(5):47-61.

32. Du L. Numerical and Experimental Investigations of Darrieus Wind Turbine Start-up and Operation. *PhD Thesis, Unverisity of Durham, UK.* 2016.

33. Du L, Berson A, Dominy RG. Aerofoil behaviour at high angles of attack and at Reynolds numbers appropriate for small wind turbines. *Proceedings of the Institution of Mechanical Engineers, Part C: Journal of Mechanical Engineering Science.* 2014;229(11):2007-2022.

34. Hill N, Dominy RG, Ingram G, Dominy J. Darrieus Turbines: the Physics of Self-starting. *Proceedings of the Institution of Mechanical Engineers, Part A: Journal of Power and Energy.* 2008;223(1):21-29.

35. Pressure System ESP User's Manual 2009. http://marmatek.com/wp-content/uploads/2014/03/Meas_ESP-HD_Manual.pdf. Accessed:Dec. 3, 2018.

36. Sims-Williams D. Self-excited Aerodynamic Unsteadiness Associated with Passenger Cars. *Dissertation, Unverisity of Durham, UK.* 2001.

37. Sims-Williams D, Luck DA. Transfer function characterization of pressure signal tubes for the measurement of large amplitude pressure fluctuations. *Proceedings of the Institution of Mechanical Engineers, Part C: Journal of Mechanical Engineering Science* 2007;221(6):707-771.

38. Anderson J, Streitlien K, Barrett DS, Triantafyllou MS. Oscillating Foils of High Propulsive Efficiency. *Journal of Fluid Mechanics.* 1998;360(360):41-72.

39. Young J. Numerical simulation of the unsteady aerodynamics of flapping airfoils *Dissertation, University of New South Wales, Australia* 2005.

40. Worasinchai S. Small Wind Turbine Starting Behaviour. *Dissertation, School of Engineering and computing science, University of Durham, UK.* 2012.

41. Migliore P, Wolfe WP, Fanucci JB. Flow Curvature Effects on Darrieus Turbine Blade Aerodynamics. *Energy.* 1980;4(2):49-55.

42. Gerakopulos R, Boutilier MSH, Yarusevych S. Aerodynamic Characterization of a NACA 0018 Airfoil at Low Reynolds Numbers. *Paper No. AIAA-2010-4629, 40th Fluid Dynamics Conference and Exhibit, 28 June - 01 July, Chicago, Illinois.* 2010.

43. Hansen K, Kelso RM, Dally BB. Performance Variations of Leading-Edge Tubercles for Distinct Airfoil Profiles. *AIAA Journal.* 2011;49(1):185-194.

44. Holst D, Church B, Pechlivanoglou G, Tuzuner E, Saverin J, Nayeri CN, Paschereit CO. EXPERIMENTAL ANALYSIS OF A NACA 0021 AIRFOIL SECTION THROUGH 180-DEGREE ANGLE OF ATTACK AT LOW REYNOLDS NUMBERS FOR USE IN WIND TURBINE ANALYSIS. *Proceedings of ASME Turbo Expo 2017: Turbomachinery Technical Conference and Exposition GT2017 June 26-30, Charlotte, NC, USA.* 2017.

45. Balduzzi F, Bianchini A, Ferrara G, Holst D, Church B, Wegner F, Pechlivanoglou G, Nayeri CN, Paschereit CO, Ferrari L. STATIC AND DYNAMIC ANALYSIS OF A NACA 0021 AIRFOIL SECTION AT LOW REYNOLDS NUMBERS BASED ON EXPERIMENTS AND CFD. *Journal of Engineering for Gas Turbines and Power.* 2018.